High-frequency ultrasonic speckle velocimetry in sheared complex fluids

Sébastien Manneville, Lydiane Bécu, and Annie Colin
Centre de Recherche Paul Pascal, Avenue Schweitzer, 33600 Pessac, FRANCE
(Dated: February 2, 2008)

High-frequency ultrasonic pulses at 36 MHz are used to measure velocity profiles in a complex fluid sheared in the Couette geometry. Our technique is based on time-domain cross-correlation of ultrasonic speckle signals backscattered by the moving medium. Post-processing of acoustic data allows us to record a velocity profile in 0.02–2 s with a spatial resolution of 40 μm over 1 mm. After a careful calibration using a Newtonian suspension, the technique is applied to a sheared lyotropic lamellar phase seeded with polystyrene spheres of diameter 3–10 μm. Time-averaged velocity profiles reveal the existence of inhomogeneous flows, with both wall slip and shear bands, in the vicinity of a shear-induced "layering" transition. Slow transient regimes and/or temporal fluctuations can also be resolved and exhibit complex spatio-temporal flow behaviors with sometimes more than two shear bands.

PACS numbers: 43.58.+z Acoustical measurements and instrumentation – 43.60.+d Acoustic signal processing – 47.50.+d Non-Newtonian fluid flows – 83.60.Wc Flow instabilities

I. INTRODUCTION

Accurate measurements of flow velocities are essential for exploring and understanding fluid dynamics. Such measurements raise important technical problems whenever one needs them to be nonintrusive. Indeed, many applications where direct access to the fluid is impossible perclude the use of local probes such as miniature piezoelectric pressure probes, hot films or hot wires. In other cases, the introduction of a probe inside the fluid may perturb the flow or even the fluid structure itself, and may lead to incorrect interpretations of the measurements. Thus, in general, much insight can be gained from some remote, noninvasive sensing of the flow field.

In the following, we focus on the case of complex fluids under simple shear. A "complex" fluid may be characterized by the existence of a "mesoscopic" length located somewhere between the size of individual molecules and the size of the sample [1]. For instance, this intermediate length scale is the particle diameter in a colloidal suspension, the diameter of an oil droplet in an emulsion, or the radius of gyration of polymer coils. The existence of such a supramolecular organization (or "microstructure") can lead to very complicated behaviors under flow and to inhomogeneous velocity profiles under simple shear [1, 2]. Since the microstructure of a complex fluid is very sensitive to local deformations, it is quite obvious that a nonintrusive technique is required in order to measure velocity profiles.

The most popular nonintrusive techniques, namely Particle Imaging Velocimetry (PIV) or Laser Doppler Velocimetry (LDV), are based on the interaction between light and seeding particles following the flow [3, 4]. However, many complex fluids, such as emulsions, slurries, or pastes, may not be transparent enough to allow the use of PIV or LDV. Nuclear Magnetic Resonance (NMR) offers the possibility to image opaque media [5, 6] but requires the use of powerful magnets and remains expensive and tricky to set up. On the other hand, ultrasound appears as an efficient, cost-effective tool to measure velocity profiles in a large range of fluids.

In this paper, we adapt a speckle-based ultrasonic velocimetry technique [7, 8] to complex fluid flows. Although based on the classical principle of backscattering by particles suspended in the flow, our technique brings an original contribution to both the fields of acoustical flow measurements and of complex fluid studies. Indeed, by using high-frequency pulses (frequencies larger than 20 MHz), we show that we are able to measure velocity profiles in complex fluids sheared between two plates separated by 1 mm with a spatial resolution of about 40 μm. Depending on the required accuracy, a full velocity profile can be obtained typically in 0.02 s to 2 s, which makes it possible to resolve transient regimes or temporal fluctuations of the flow.

The paper is organized as follows. We first explain in more details why local velocity measurements are crucial to the understanding of complex fluids. Examples are given that show that inhomogeneous flows may occur even in simple shear geometries and at small imposed stresses. The third section is devoted to a brief review of existing ultrasonic techniques for measuring flow velocities. We then present the electronic setup and the data analysis used for high-frequency ultrasonic speckle velocimetry (USV). Section V deals with the calibration step necessary to obtain quantitative estimates of the velocity. In Section VI, high-frequency USV is applied to a particular complex fluid: an aqueous solution of surfactant. The ultrasonic data reveal the existence of inhomogeneous flows, with both wall slip and shear bands, as well as complex spatio-temporal behaviors during transient regimes. Finally, in light of the present results, the technique is compared to other nonintrusive tools used in the field of complex fluid flows. We emphasize on the promising spatio-temporal resolution of USV and discuss its possible future applications.

II. SHEAR FLOW OF COMPLEX FLUIDS: WHY ARE LOCAL MEASUREMENTS ESSENTIAL?

A. Shearing a Newtonian fluid in the Couette geometry

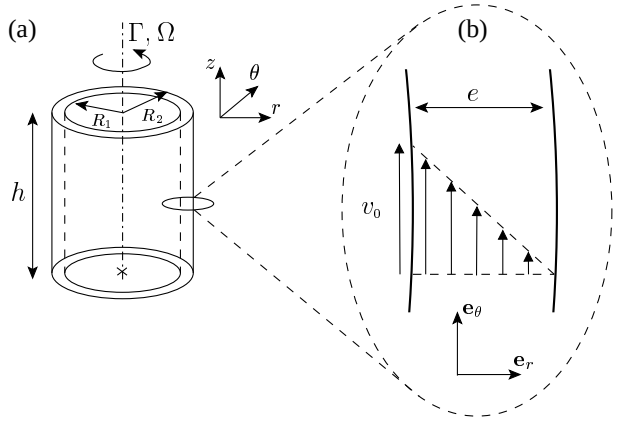

FIG. 1: (a) Sketch of the Couette cell used in our experiments. (b) Enlargement of the shear flow inside the gap between the two cylinders in the case of a Newtonian fluid below the onset of the Taylor-Couette instability.

It is well-known that shear flows of simple fluids are laminar at low velocities and may become unstable above a critical Reynolds number due to hydrodynamic instabilities [9]. A classical shear geometry is the *Couette geometry* in which the fluid is sheared between two concentric cylinders as sketched on Fig. 1. Usually the inner cylinder of radius R_1 is rotating while the outer cylinder of radius R_2 remains fixed. The two cylinders are thus called "rotor" and "stator" respectively. The distance $e = R_2 - R_1$ between the two walls is called the "gap" of the Couette cell. This Couette geometry will be used throughout the paper as well as the cylindrical coordinates (r, θ, z). We will denote $x = r - R_1$ the distance from the inner cylinder and $\mathbf{v} = (v_r, v_\theta, v_z)$ the velocity vector.

A Couette device can work in two different modes: either a torque Γ is imposed on the rotor and the rotor angular velocity Ω is measured, or Ω is imposed and the torque Γ is measured. For a Newtonian fluid at small velocities, the flow is stationary and purely orthoradial $\mathbf{v} = (0, v_\theta(r), 0)$. The tangential velocity $v(x) \equiv v_\theta(r)$ decreases from the rotor velocity $v_0 = R_1\Omega$ down to zero on the outer wall. In the small gap approximation *i.e.* when $e \ll R_1$, the velocity profile is linear as shown in Fig. 2(a). The shear rate $\dot\gamma$ ($r\theta$-component of the rate-of-strain tensor) and the shear stress σ (tangential force per unit surface *i.e.* $r\theta$-component of the stress tensor) are then almost uniform across the gap and are simply given by:

$$\dot\gamma \equiv r\frac{\partial(v_\theta/r)}{\partial r} = \frac{R_1\Omega}{e} = \frac{v_0}{e}\,, \tag{1}$$

$$\sigma = \frac{\Gamma}{2\pi R_1 H}\,, \tag{2}$$

where H is the height of the Couette cell. The viscosity η of the sample can thus be computed from the rheological data $\dot\gamma$ and σ by $\eta = \sigma/\dot\gamma$, as long as the flow remains laminar and stationary.

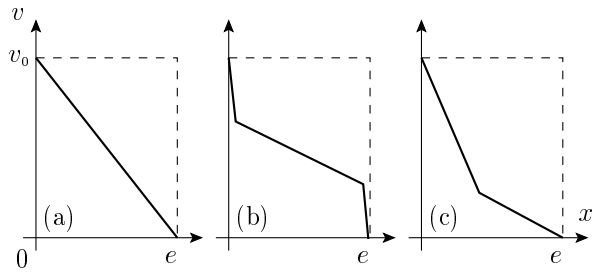

FIG. 2: Examples of orthoradial velocity profiles observed in a small gap Couette geometry. (a) Newtonian fluid sheared below the onset of the Taylor-Couette instability. (b) Wall slip in a complex fluid: apparent slippage results from the presence of thin lubricating layers near the walls. (c) Shear banding in a complex fluid near a shear-induced transition: two differently sheared bands coexist in the gap of the cell.

B. Inhomogeneous flows in sheared complex fluids

1. *Apparent wall slip*

In complex fluids, the picture of the Couette flow may be radically different. For instance, when a complex fluid is confined between two plates and depending on the roughness properties of the plates, the fluid velocity close to the walls may strongly differ from that of the walls (see Fig. 2(b)): the fluid *slips*. Slippage is usually explained by the existence of two thin lubricating layers in which the fluid structure is very different from that in the bulk. For instance, in a colloidal suspension, electrostatic or steric effects next to the walls may induce a depletion of the particles on a small distance, leaving a much less viscous fluid film at the walls and leading to this apparent wall slip [10]. In concentrated oil-in-water emulsions, wall slip is due to the presence of very thin water layers close to the walls.

Even if the bulk fluid remains Newtonian, the velocity profile between the two plates may be quite different from that expected in a uniformly sheared fluid that does not slip (see Fig. 2(a)). Wall slip in complex fluids raises important industrial problems and is often difficult to detect and to assess quantitatively. In particular, computing the viscosity from Eqs. (1) and (2) can be very

misleading since the effective shear rate in the bulk is sometimes orders of magnitude smaller than v_0/e [10].

2. Hydrodynamic and elastic instabilities

Moreover, even in the absence of wall slip and even for Newtonian fluids, above a critical rotation speed of the rotor, the laminar flow becomes unstable and vortices develop due to the centrifugal force (*Taylor-Couette instability*). Upon further increasing the rotation speed, this three-dimensional, inhomogeneous but still stationary flow turns into a time-dependent turbulent flow [9]. The procedure based on Eqs. (1) and (2) for measuring $\dot{\gamma}$ and σ and computing the viscosity then completely fails because the flow is no longer laminar and stationary.

About fifteen years ago, complex fluids such as entangled polymer solutions were shown to present inhomogeneous flows even when sheared at rotor velocities far below the onset of the Taylor-Couette instability. These unstable flows result from purely *elastic instabilities* [11, 12]. Although due to the elasticity of the fluid rather than visco-inertial effects, the phenomenology of such instabilities is very similar to classical hydrodynamic instabilities but occur at very low Reynolds numbers.

3. Shear-induced structures and shear-banded flows

Beside those inertial and elastic instabilities, more subtle effects may come into play that are due to the very nature of complex fluids. Indeed, application of shear to a complex fluid may completely change its microstructure leading to a new *shear-induced structure*. Such a phenomenon may be called a *shear-induced transition* or a *material instability* in the sense that it results from a strong coupling between the shear flow and the microstructure of the fluid [13].

A material instability usually shows up on rheological data as a sudden jump in the viscosity when shear is increased. For instance, if the shear-induced structure is much less viscous than the complex fluid at low shear, then a large drop of the visocity may be observed and the transition is called a shear-thinning transition. During such a transition, the fluid is assumed to phase-separate into two states: a shear-induced state that flows at a given shear rate and coexists with the old structure, thus giving rise to two shear bands [14, 15, 16]. The corresponding *shear-banded* velocity profile is sketched in Fig. 2(c).

In order to investigate those transitions, most previous studies have focused on global measurements such as the viscosity of the sample as a function of time [17, 18, 19]. Indeed, the time series $\eta(t)$ sometimes display complex temporal fluctuations on time scales characteristic of the microstructure rearrangements. However, such global measurements do not provide any information on the spatial structure of the flow [20]. Thus, other studies have focused on the local characterization of the fluid structure using birefringence neutron, x-ray or light scattering and showed the coexistence of bands of different microstructures in the vicinity of shear-induced transitions [21, 22, 23].

As far as the flow field is concerned, rather few local velocity measurements are reported in the complex fluid literature [2, 24]. The presence of inhomogeneous flows in some surfactant mixtures ("wormlike micelles") was first unveiled using NMR [25, 26]. However, the existence of shear bands in the velocity profiles was firmly ascertained only recently using dynamic light scattering (DLS) in heterodyne mode, a technique close to LDV [27, 28].

From the various examples cited above, it is quite clear that local measurements are essential, for instance to precisely follow the shear bands in both space and time. In general, a velocity profile with about 20 points accross a 1 mm gap, *i.e.* with a resolution of 50 μm, will carry enough spatial information on the flow to allow quantitative conclusions on possible inhomogeneous flow profiles.

III. MEASURING FLUID FLOWS WITH ULTRASOUND: A SHORT REVIEW

A. Continuous wave systems

Contrary to electromagnetic waves, the *phase* of acoustic waves is easily accessible using piezoelectric transducers. Moreover, ultrasound may propagate deeply into optically opaque media. These two properties have led to the spectacular development of ultrasonic imaging techniques since the early 1950s particularly in the *biomedical* domain.

When an ultrasonic wave travels through biological tissues, it gets scattered by density and/or compressibility inhomogeneities [29]. If the scatterer moves in a flow, like for instance red blood cells inside blood vessels, its motion induces a Doppler shift in the wave frequency. Early systems for measuring blood velocities were based on the estimation of this Doppler frequency shift using a monochromatic ultrasonic wave [8].

Unfortunately, even if these "true Doppler" systems helped to detect the occlusion of blood vessels, they did not offer any spatial resolution. Indeed, if one uses a continuous wave, one gets a very good resolution on the frequency shift (and thus on the velocity) but one also loses any temporal information on the echo arrival time (and thus on the scatterer position, as explained below). Continuous Doppler systems may thus be very efficient in the case of a single scatterer suspended in a flow whose position is measured independently [30].

B. Pulsed wave systems

In order to discriminate between different scatterers in space and to measure velocity profiles, a solution is to

use short acoustic *pulses*. Indeed, if an ultrasonic pulse is sent by a transducer through a scattering medium, a series of backscattered echoes can be recorded on the same transducer. The precise nature of the backscattered (BS) signal will be discussed at length in Sec. IV. At this point, it is only important to note that the arrival times t_k of the echoes are directly linked to the position y_k of the scatterer along the acoustic beam by $y_k = c_0 t_k/2$, where c_0 is the effective sound speed and the factor 2 accounts for the round trip from the transducer to the k^{th} inhomogeneity and back to the transducer.

The idea is then to follow the scatterer motion through the evolution of the BS signals: between successive pulses, echoes will move along with the flow and their positions may be tracked in time. Although the Doppler effect is not used in pulsed wave systems, these are still mistermed "pulsed Doppler systems" in the literature and the technique is referred to as "ultrasonic Doppler velocimetry" (UDV) or "ultrasonic velocity profiler" (UVP) [31]. This confusion may be due to the fact that, owing to the constraint of real-time display in commercial devices, BS signals are sampled only at a few given depths and that these sampled signals are analyzed in the frequency domain [8].

UDV has been successfully applied to various classical problems in hydrodynamics such as the Taylor-Couette instability [32], cylinder wakes [33], or magnetic fluid flows [34]. The fluid has to be seeded with small particles that scatter ultrasound. Such acoustic "contrast agents" are assumed to follow the flow as Lagrangian tracers. The UVP has also been used fairly recently for in-line rheological studies of concentrated suspensions in pipe flows [35].

If one drops the constraint of real-time display, the whole BS signals may be stored for post-processing. Direct tracking of the BS signals in the time domain is the subject of recent technical developments such as ultrasonic speckle velocimetry which will be addressed in the next Section.

IV. HIGH-FREQUENCY ULTRASONIC SPECKLE VELOCIMETRY

A. Speckle tracking techniques

When the moving medium contains a lot of scatterers per unit volume, the BS signal results from the interferences of all the backscattered waves and appears as a complex, high-frequency signal called *ultrasonic speckle* (see Fig. 5 for a typical speckle signal and Sec. IV D for more details, in particular about the possibility of multiple scattering). The development of fast digitizers with large memories has allowed the full recording of backscattered BS signals for post-processing. Various time-domain algorithms for tracking the motion of ultrasonic echoes have been proposed [36, 37, 38, 39, 40]. So far, such *speckle tracking* techniques have mainly been applied to the measurement of tissue motion or blood flow [7, 8]. They have also been adapted to the UVP system and tested on pipe flows to provide high time resolution (of about 0.5 ms per profile) [41]. Recently, one of us introduced a combination of a 2D echographic system and speckle tracking that we called 2D ultrasonic speckle velocimetry (USV) [42]. This system allowed us to image strong vortical flows in Newtonian fluids in two dimensions [43].

Here we propose to adapt such a technique to complex fluids confined in a Couette cell of gap $e \simeq 1$ mm. As explained in Section II B, one needs to measure velocity profiles with a spatial resolution of typically 50 μm. However, frequencies commonly used in commercial ultrasonic velocimeters are in the range $f = 1$–10 MHz, and with a typical sound speed $c_0 \simeq 1500$ m.s^{-1}, this yields a resolution of about $\lambda = c_0/f \simeq 0.15$–$1.5$ mm. Thus, conventional ultrasound does not permit very fine measurements and one has to turn to utrasound with frequencies larger than 20 MHz. Again, high frequencies have first attracted the biomedical community. High-resolution ultrasonic images have been recently obtained in dermatology, ophtalmology and stomatology [44, 45] or for measuring blood flow in the microcirculation [46, 47]. To our knowledge, no such high-frequency measurements (above 20 MHz) have been reported so far in classical hydrodynamics nor in the field of complex fluids.

Note that the resolution cannot be increased indefinitely by increasing the frequency because *attenuation* of sound waves sharply increases with frequency (as f^2 in water). Attenuation is due to the combination of thermoviscous absorption and scattering. The signal-to-noise ratio rapidly deteriorates as f increases. We found that for our application to complex fluids, $f = 36$ MHz realizes a good compromise between resolution and attenuation over propagation distances of a couple of centimeters. Finally, since transducer arrays are not available at such a high frequency, the technique will have to be restricted to one-dimensional measurements.

B. High-frequency USV electronic system

Figure 3 presents our USV electronic system. Focused ultrasonic pulses are generated by a PVDF piezo-polymer immersion transducer of central frequency $f = 36$ MHz (Panametrics PI 50-2). The focal distance is 11.6 mm and the active element diameter is 6.3 mm. The transducer bandwidth is 11 MHz at -3 dB. The axial and lateral resolutions given by the manufacturer at -3 dB are 30 μm and 65 μm respectively and the depth of field is about 1 mm.

The transducer is controlled by a pulser-receiver unit (Panametrics 5900PR). The pulser generates 220 V pulses with a rise time of about 1 ns. The pulse repetition frequency (PRF) is tunable from 0 to 20 kHz. The receiver is equipped with a 200 MHz broadband amplifier of maximum voltage gain 54 dB as well as a

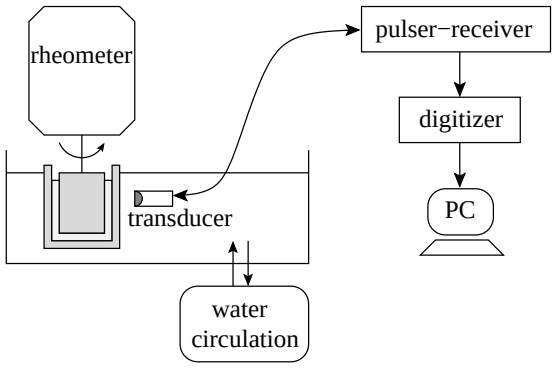

FIG. 3: Electronic system used for high-frequency USV.

set of selectable high-pass and low-pass filters. BS signals are sampled at $f_s = 500$ MHz, stored on a high-speed PCI digitizer with 8 Mb on-board memory (Acqiris DP235), and later transferred to the host computer for post-processing.

C. Experimental setup in the Couette geometry

The shear flow is generated in a Plexiglas Couette cell with $R_1 = 24$ mm, $R_2 = 25.07$ mm, and $H = 30$ mm. The rotation of the inner cylinder is controlled by a standard rheometer (TA Instruments AR1000). The whole cell is surrounded by water whose temperature is kept constant to within ± 0.1°C. The thickness of the stator is 2 mm everywhere except for a small rectangular window where the minimal thickness is 0.5 mm in order to avoid additional attenuation due to the Plexiglas.

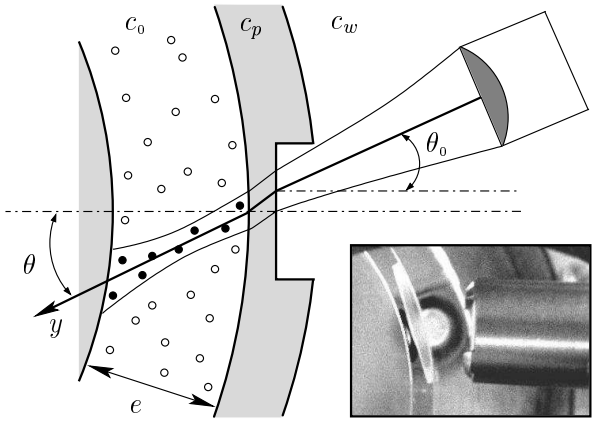

FIG. 4: Experimental setup for USV in complex fluids sheared in the Couette geometry. c_0, c_p, and c_w stand for the speed of sound in the complex fluid, in Plexiglas, and in water respectively. The inset shows a picture of the transducer and the stator as seen from above once the rotor has been removed.

Ultrasonic pulses are incident on the stator with a given angle $\theta_0 \simeq 20°$ relative to the normal to the window in the stator as sketched in Fig. 4. They travel through Plexiglas and enter the gap with an angle θ that is given by the law of refraction. Since the sound speed of the working fluid may differ from that of water, and since the precise value of θ depends on the exact arrangement of the acoustic beam relative the stator, θ will be taken as an unknown until a careful calibration procedure is completed (see Section V).

Once inside the fluid, ultrasonic pulses get scattered by inhomogeneities that can be either naturally present (oil droplets in an emulsion for instance) or artificially introduced to enhance the acoustic contrast. The total round trip for a pulse travelling from the transducer to the rotor and back to the transducer lasts about 15 μs.

The position of the transducer is tuned so that the 1 mm gap lies into the focal spot in order to optimize the signal-to-noise ratio. Typical recorded BS signals are 1000 point long, which corresponds to a transit time of 2 μs or equivalently to a depth of roughly 1.5 mm inside the medium. Allowing for a fraction of a millimeter before the stator and after the rotor helps to locate the two walls. Note that spurious reflections on water–Plexiglas or Plexiglas–fluid interfaces are minimized by carefully choosing the angle θ_0. In any case, even in the absence of interfaces, such an angle is necessary to get a non-zero projection of the velocity vector along the acoustic axis as explained below.

D. Data analysis involved in USV

1. Basic principle of USV

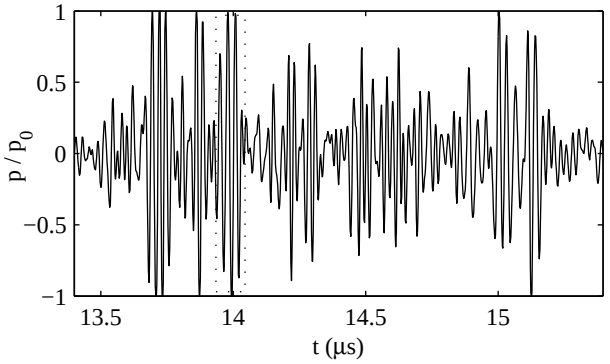

FIG. 5: Speckle signal recorded in a 1 % wt. suspension of polystyrene spheres. The voltage $V(t)$ from the transducer output is directly proportional to the pressure $p(t)$. The signal was normalized by its maximum value V_0, which yields $V/V_0 = p/p_0$ where p_0 is the maximum pressure. The sampling frequency is $f_s = 500$ MHz and the recorded signal is 1000 point long. The rotor velocity is $v_0 = 23.5$ mm.s^{-1}. The dotted rectangle denotes the time window used in Figs. 6 and 7.

Figure 5 shows a typical signal backscattered by a di-

lute suspension of polystyrene spheres and normalized by the maximum amplitude. The noise level is about 10 mV in all our experiments and typical signal amplitudes are in the range 50–200 mV corresponding to a signal-to-noise ratio of 10–30 dB.

Under the assumption of *single scattering*, the speckle signal received between times t and $t+\Delta t$ can be interpreted as interferences coming from scatterers located between y and $y+\Delta y$, where $y = c_0 t/2$, $\Delta y = c_0 \Delta t/2$, and y is the distance from the transducer along the acoustic beam. The approximation that no multiple scattering takes place is thus essential in order to use the echographic conversion rule $y = c_0 t/2$. Multiple scattering is avoided by carefully controlling the amount and the properties of the scatterers (see Sec. V).

When the fluid is submitted to a shear flow, the interference pattern changes as the scatterers move along. Figure 6 shows two signals corresponding to two pulses separated by $\delta T = 1$ ms and plotted over 4 acoustic periods. A global shift to the right of $\delta t \simeq 3$ ns is clearly visible. With $c_0 \simeq 1500$ m.s^{-1}, this corresponds to $\delta y = c_0 \delta t/2 \simeq 2$ μm and to a velocity $v_y = \delta y/\delta T \simeq 2$ mm.s^{-1} projected along the acoustic axis.

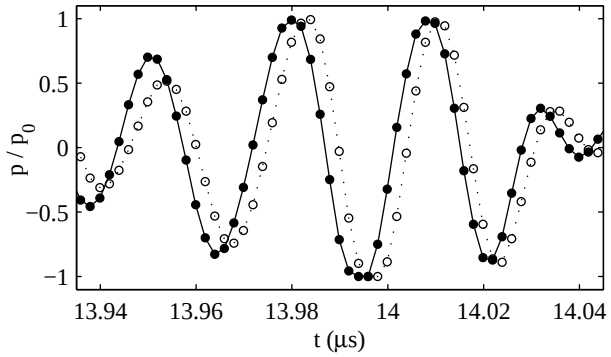

FIG. 6: Zoom over 4 acoustic periods of the speckle signal p/p_0. Bullets (•) correspond to the speckle signal p_T shown in Fig. 5 received after a pulse is sent at time T. Open circles (∘) correspond to the signal $p_{T+\delta T}$ recorded over the same time window after a second pulse is sent 1 ms later at $T+\delta T$ and when shear is applied. The motion of the scatterers result in a shift to the right of the signal *i.e.* the scatterers move away from the transducer. The rotor velocity is $v_0 = 23.5$ mm.s^{-1}.

2. *Cross-correlation algorithm*

In order to get an accurate estimate of the time-shift δt, we use the simple cross-correlation algorithm described below. Two consecutive signals p_T and $p_{T+\delta T}$ recorded after pulses sent at times T and $T+\delta T$ are cross-correlated over small time windows of width $\Delta t = 4t_{\rm ac} \simeq 0.11$ μs, where $t_{\rm ac} = 1/f$ is the acoustic period. More precisely, the following cross-correlation coefficient is computed according to:

$$C_k(\tau) = \sum_{t'=t_k-\Delta t/2}^{t_k+\Delta t/2} p_T(t')\, p_{T+\delta T}(t'+\tau)\,, \qquad (3)$$

where the $k^{\rm th}$ time window is centered around $t_k = t_s + k\Delta t/2$ and $t_s \simeq 13.5$ μs is a reference time that corresponds to the beginning of the gap. t_s depends on experimental parameters such as the working temperature and on the exact arrangement of the transducer relative to the Couette cell (see Sec. V). The times t_k correspond to the centers of the various time windows over which the signals are split. They will be later converted into positions y_k at which the velocity is measured using $y_k = c_0(t_k - t_s)/2$. Such windows correspond to slices of width $\Delta y = 2\lambda \simeq 80$ μm along the acoustic axis separated by $\Delta y/2 \simeq 40$ μm.

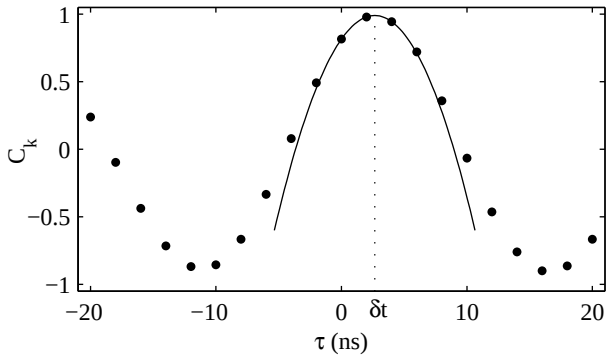

FIG. 7: Correlation function $C_k(\tau)$ obtained by using Eq. (3) on the two signals of Fig. 6 (•). The solid line corresponds to the parabolic interpolation $\tilde{C}_k(\tau)$ and the dotted line indicates the position $\delta t \simeq 2.7$ ns of the maximum of $\tilde{C}_k$.

As shown in Fig. 7, the correlation function $C_k(\tau)$ is then interpolated around its main maximum by a parabola and the value δt of τ that maximizes this parabola is extracted:

$$\tilde{C}_k(\delta t) = \max_{\tau} \left(\tilde{C}_k(\tau) \right)\,, \qquad (4)$$

where $\tilde{C}_k$ denotes the parabolic interpolation of C_k. Note that δt depends both on the position t_k of the time window (fast "ultrasonic time") and on the time T for which the cross-correlation is performed (slow "pulse time"). Thus δt will be noted as a function of the two variables t_k and T below.

Finally, it is straightforward to convert time-shifts δt into velocities using:

$$v_y(y_k, T) = \frac{c_0}{2}\, \frac{\delta t(t_k, T)}{\delta T}\,, \qquad (5)$$

where

$$y_k = c_0(t_k - t_s)/2 \qquad (6)$$

is the position of the center of the window along the acoustic axis. The origin $y = 0$ is taken at the stator–fluid interface. Equation (5) thus yields the projection v_y of the velocity vector along the acoustic axis at the discrete positions y_k and at time T.

3. Limits of the technique

The procedure based on the interpolation of $C_k(\tau)$ allows us to measure time-shifts as small as $\delta t \simeq 0.2$ ns that correspond to displacements $\delta y \simeq 0.15$ μm. Since the PRF $f_{\text{PRF}} = 1/\delta T$ can be made as small as desired, infinitesimal velocities could in principle be measured. However, at very small shear rates, decorrelation of the BS signals may occur due to Brownian motion of the scatterers or to low-frequency mechanical vibrations in the experimental setup. Consequently, we will avoid using PRFs smaller than 10 Hz and we estimate the minimum measurable velocity at about 1 μm.s^{-1}.

On the other hand, the maximum measurable velocity is reached when $\delta y \simeq \lambda \simeq 40$ μm. Indeed, displacements greater than the acoustic wavelength cannot be measured using the cross-correlation algorithm described above unless phase unwrapping and continuity conditions are implemented, which will not be considered here [43]. With the highest achievable PRF $f_{\text{PRF}} = 20$ kHz, a 40 μm maximum displacement means that velocities above 0.8 m.s^{-1} may not be accessed using USV. Note however that this limiting range of [1 μm.s^{-1} – 0.8 m.s^{-1}] applies to the velocity v_y projected along the acoustic axis. This range may be extended by varying the incidence angle θ (see Sec. V D and Eqs. (8)–(9) below).

Finally, Eq. (5) shows that a velocity profile could in principle be obtained by cross-correlating only two successive BS signals *i.e.* within a time interval δT that can be made very small depending of the PRF. In practice, as seen on Fig. 5, the speckle amplitude is never uniform. Locally, destructive interferences or the absence of scatterers may lead to signal levels too small to be analyzed (see the signal of Fig. 5 around $t \simeq 14.1$ or 14.4 μs for instance). Time windows where the signal amplitude does not reach a given threshold (typically 20 % of the maximum amplitude) are thus left out of the analysis. To recover a full velocity profile, some averaging is then performed over several sucessive cross-correlations:

$$v_y(y_k) = \langle v_y(y_k, T) \rangle_T \ . \tag{7}$$

Figure 8 shows twenty successive BS signals recorded in a sheared Newtonian suspension with $f_{\text{PRF}} = 1$ kHz. The ultrasonic pulses leave the stator and enter the gap at $t_s \simeq 13.5$ μs and a small fixed echo corresponding to the rotor position may be seen at $t_r \simeq 15.0$ μs (as well as a stronger echo at about 15.2 μs that corresponds to a multiple reflection from the Plexiglas window in the stator). The slopes of the traces left by the echoes in this two-dimensional (t, T) diagram are inversely proportional to the local velocities according to Eq. (5). Thus,

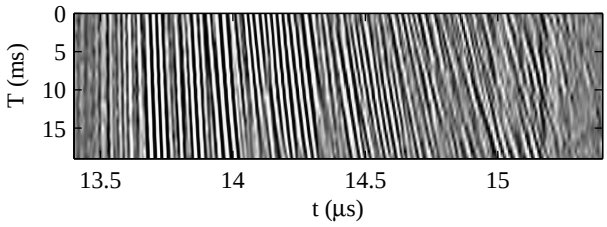

FIG. 8: BS signals corresponding to 20 pulses sent every $\delta T = 1$ ms. The normalized pressure p/p_0 is coded in gray levels. In order to highlight the areas with strong speckle signal, the colormap was saturated so that white (black resp.) corresponds to $p/p_0 \geq 0.4$ (≤ -0.4 resp.). Time windows where $\max(|p/p_0|) < 0.2$ are not taken into account in the data analysis (see text). The gap lies between $t_s \simeq 13.5$ μs and $t_r \simeq 15.0$ μs. The horizontal axis is the fast "ultrasonic time" t and the vertical axis is the slow "pulse time" T. The rotor velocity is $v_0 = 23.5$ mm.s^{-1}.

the signature of shear is rather clear: velocities increase from the stator, where the scatterers remain almost fixed, to the rotor. Moreover, the presence of moving echoes for times $t > t_r$ is not surprising: these echoes simply correspond to scattering of the wave reflected on the rotor. One can see that the whole range of times from t_s to t_r gets covered by some significant speckle signal in about 20 ms in that case.

If better accuracy is required, more averaging can be performed to improve the statistical convergence of the method (see Fig. 13 below). Depending on the tradeoff between accuracy and temporal resolution, we found that USV allows us to obtain a full velocity profile every 0.02–2 s.

V. CALIBRATION PROCEDURE USING A NEWTONIAN FLUID

A. Newtonian suspension of "contrast agents"

In order to test and calibrate the experiment, much effort was devoted to developing "contrast agents" that feature good scattering properties for high-frequency USV. Indeed, too weak a scatterer yields a signal level too low to work with, whereas too strong a scatterer leads to multiple scattering. When the scatterer is small compared to the acoustic wavelength (Rayleigh approximation), three parameters control the amount of scattering: the scatterer diameter, its compressibility and its density [29]. Moreover, if one wants the contrast agents to remain Lagrangian tracers of the flow, their density has to be matched to that of the fluid.

We found that homemade polystyrene spheres of diameter $a = 3$–10 μm were large and hard enough to scatter 36 MHz pulses efficiently but soft enough to prevent multiple scattering when diluted at a weight concentration

of 1 % in water. Such polystyrene spheres were obtained by polymerization following Refs. [48, 49]. A 1 % wt. solution of benzoyl peroxide in divynylbenzene is first prepared. Then, a polydisperse emulsion is obtained by stirring 40 g of the previous mixture in 59 g of water and 1 g of sodium dodecyl sulfate at room temperature. Finally, the emulsion is polymerized at 90°C for two hours. The prepared polystyrene spheres were washed with water three times before drying. The 1 % wt. suspension of such polystyrene spheres is Newtonian and has the same viscosity as water.

B. Measurement of c_0

In order to use Eqs. (5) and (6), the sound speed c_0 of the working fluid has to be measured. We used a classical *transmission* setup consisting of two transducers facing each other. One of them, the emitter, remains fixed while the other works as a receiver and can be moved by a computer-controlled actuator. Pulses are recorded for various displacements δy of the receiver and averaged over 100 sweeps. The time-shifts δt between the arrival times of the pulses are measured and the sound speed c_0 is given by the slope of δy vs. δt (see Fig. 9).

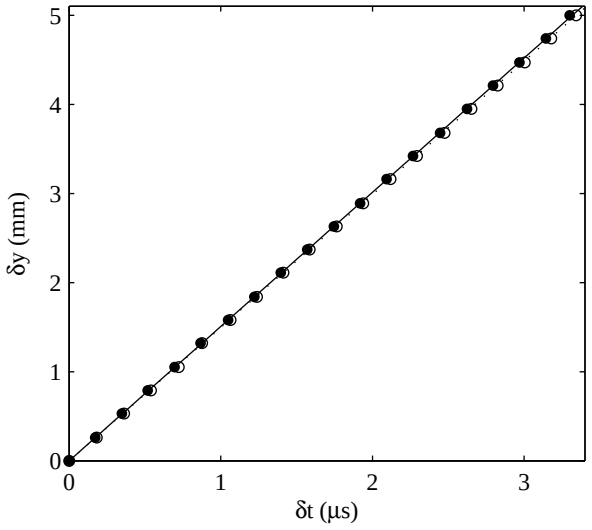

FIG. 9: Measurement of the sound speed c_0 as the slope of δy vs. δt (see text) for the Newtonian 1 % wt. suspension of polystyrene spheres (•) and for the seeded lamellar phase of Sec. VI (○). Both data sets were obtained at 32°C and $\delta y = 0$ corresponds to a separation of about 10 mm between the emitter and the receiver. Linear fits yield $c_0 = 1507 \pm 10$ m.s^{-1} for the Newtonian suspension (solid line) and $c_0 = 1495 \pm 10$ m.s^{-1} for the lamellar phase (dotted line). In practice, those two fits are almost undistinguishable. Typical errorbars on δt are about the size of the symbols.

Due to technical constraints, the measurements of c_0 were performed with 25 MHz transducers. Temperature is controlled to within 0.1°C by a water circulation around the sample. Figure 9 shows that $c_0 = 1500$ m.s^{-1} leads to a very good approximation of the data obtained in the suspension of polystyrene spheres at our working temperature of 32°C. This value of c_0 is in good agreement with the measurements reported in the literature for the sound speed of water vs. temperature [29]. In the following, we will assume that this value does not vary significantly with frequency between 25 and 36 MHz and all the data will be taken at the same temperature of 32°C.

Finally, note that the measurement of c_0 using the transmission of ultrasonic pulses between two transducers also allows us to check that no significant multiple scattering takes place in our fluids by looking at the transmitted waveform : the received signal remains always as short as the emitted pulse and no long-lasting echoes typical of multiply scattered waves were ever recorded during the measurements of c_0.

C. Measurement of t_s

Another important parameter is t_s that gives the position of the stator–fluid interface and strongly depends on the experimental conditions.

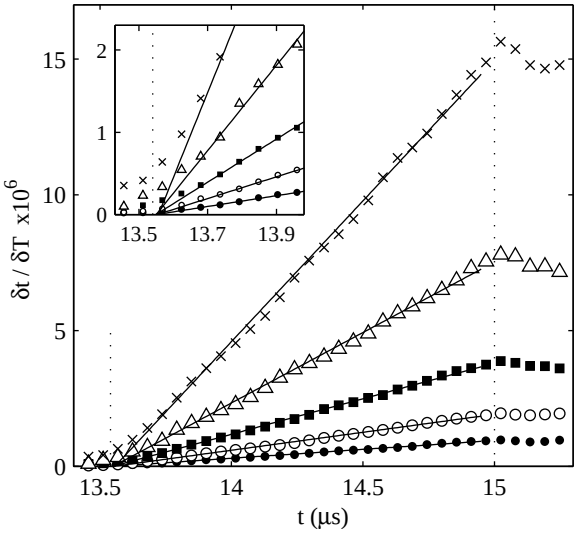

FIG. 10: $\delta t/\delta T$ as a function of the position t of the correlation window obtained in the Newtonian suspension for $v_0 = 2.9$ (•), 5.8 (○), 11.7 (■), 23.5 (△), and 47.0 mm.s^{-1} (×). The solid lines are the best linear fits of the data for $13.55 < t < 14.95$ μs. The dotted lines indicate the Plexiglas–fluid interfaces at the stator (left) and at the rotor (right). The results were averaged over 50 series of 20 pulses. Typical standard deviations are of the order of the marker size. Inset: blow-up of $\delta t/\delta T$ vs. t close to the stator.

Figure 10 presents the results of our speckle tracking algorithm averaged over 50 series of 20 pulses like that

shown in Fig. 8. The rotor velocity v_0 was varied between 2.9 and 47.0 mm.s^{-1}. The linear behavior of the time-shift δt with the position t of the correlation window is a direct signature of the uniform shear flow inside the Newtonian suspension. Indeed, all the velocities considered here are far below the onset of the Taylor-Couette instability which occurs when $v_0\, e^{3/2}/\nu R_1^{1/2} \simeq 41$ (where $\nu \simeq 10^{-6}$ m^2.s^{-1} is the kinematic viscosity of our calibration fluid) [9] *i.e.* when $v_0 \simeq 200$ mm.s^{-1}.

For our dilute suspension, no wall slip is expected and δt should go to zero at the stator: $\delta t(t_s) = 0$. By linearly fitting $\delta t/\delta T$ vs. t for various values of v_0, different estimates of t_s are obtained that yield an average value $t_s = 13.54 \pm 0.02$ μs. The uncertainty on t_s is due to the presence of the stator which leads to a small fixed echo on the signals and to small edge effects around t_s (see inset of Fig. 10). It corresponds to an uncertainty of about 15 μm on the position of the stator–fluid interface.

D. Conversion to orthoradial velocity profiles $v(x)$

Inserting the values of c_0 and t_s found above in Eqs. (5) and (6) yields the velocity profile $v_y(y)$. Thus, so far, we obtained measurements of the velocity vector projected along the acoustic axis. In order to get some physically more relevant information, we will assume from now on that the radial velocity is zero (or at least negligible when compared to the orthoradial velocity). This is of course the case for our Newtonian suspension below the onset of the Taylor-Couette instability. In complex fluids, inhomogeneous flows with wall slip or shear banding are purely orthoradial (see Sec. II B) so that the above approximation remains valid as long as hydrodynamic or elastic instabilities do not occur. Note that in the geometry discussed here, USV measurements are not affected by a non-zero vertical component of the velocity field.

Assuming that $\mathbf{v} = (0, v, 0)$ and using standard trigonometric relations (see Fig. 11), one gets:

$$v(x) = \frac{R_1 + x}{R_2 \sin\theta}\, v_y(y)\,, \tag{8}$$

where

$$x = \sqrt{R_2^2 + y^2 - 2R_2 y\cos\theta} - R_1\,. \tag{9}$$

In the small gap approximation, Eqs. (8) and (9) reduce to $v(x) \simeq v_y/\sin\theta$ and $x \simeq e - y\sin\theta$.

Thus the last parameter to calibrate is the angle θ. This is done by looking for a value of θ for which $v(x)$ coincides with the velocity profile expected for a Newtonian fluid:

$$v(x) = v_0\left(1 + \frac{x}{R_1}\right)\left[\frac{\left(\frac{R_2}{R_1+x}\right)^2 - 1}{\left(\frac{R_2}{R_1}\right)^2 - 1}\right] \simeq v_0\left(1 - \frac{x}{e}\right)\,, \tag{10}$$

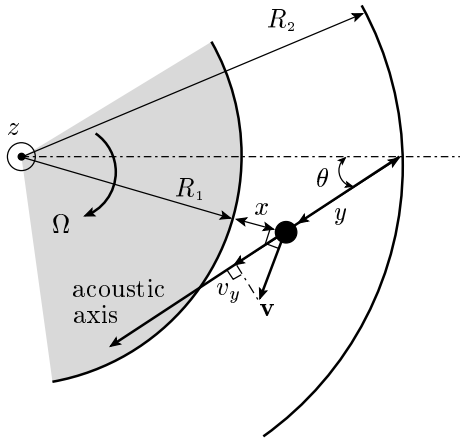

FIG. 11: Conversion of $v_y(y)$ to $v(x)$ in the Couette geometry. The flow is assumed to be purely orthoradial. x is the radial distance from the rotor whereas y is the distance from the stator–fluid interface along the acoustic axis. The gap width was exaggerated to reveal curvature effects accounted for by Eqs. (8) and (9).

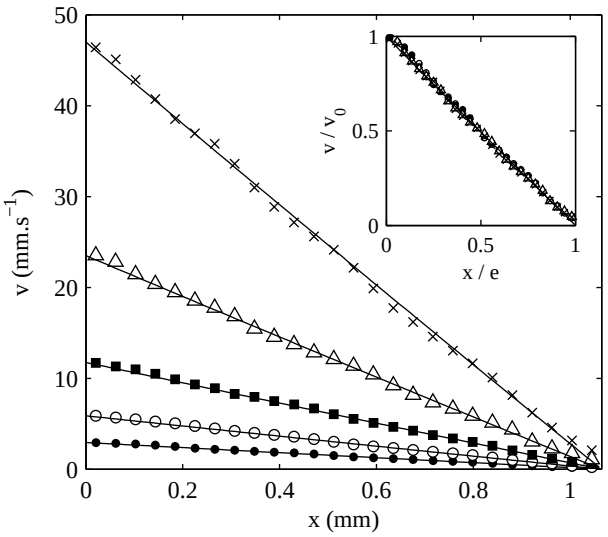

FIG. 12: Velocity profiles $v(x)$ obtained from Eqs. (8) and (9) for the data of Fig. 10 with $c_0 = 1500$ m.s^{-1}, $t_s = 13.54$ μs, and $\theta = 13.5°$. Rotor velocities are $v_0 = 2.9$ (•), 5.8 (○), 11.7 (■), 23.5 (△), and 47.0 mm.s^{-1} (×). The solid lines correspond to the Newtonian velocity profiles given by Eq. (10) with the above values of v_0. Inset: dimensionless data v/v_0 vs. x/e.

where the last term results from the small gap approximation.

Figure 12 shows that $\theta = 13.5°$ leads to very good results for all the rotor velocities v_0 considered here. Normalized data v/v_0 vs. x/e show that the Newtonian velocity profiles $v \simeq v_0(1 - x/e)$ are recovered for all our data with the set of parameters c_0, t_s, and θ inferred

from the above calibration (see inset of Fig. 12). This calibration method is very sensitive to small variations of θ and allows its estimation to within 0.2°. Note that θ depends on both the temperature and the nature of the fluid under study through c_0. As long as the temperature remains the same, the new value θ' of the incidence angle in a fluid whose sound speed c_0' differs from that of the calibration fluid is simply given by Snell's law:

$$\sin\theta' = \frac{c_0'}{c_0}\sin\theta\,, \tag{11}$$

where c_0 and θ are the parameters measured for the calibration fluid.

E. Statistical convergence of the USV measurements

Finally, Fig. 13 shows the value of the v_y measured at two different positions along the acoustic beam as more and more averaging is performed. It is clear that convergence is reached when $N \simeq 300$ pulses are taken into account. The standard deviation of the measurements decreases from about 6 % for $N \simeq 100$ to less than 3 % for $N > 400$.

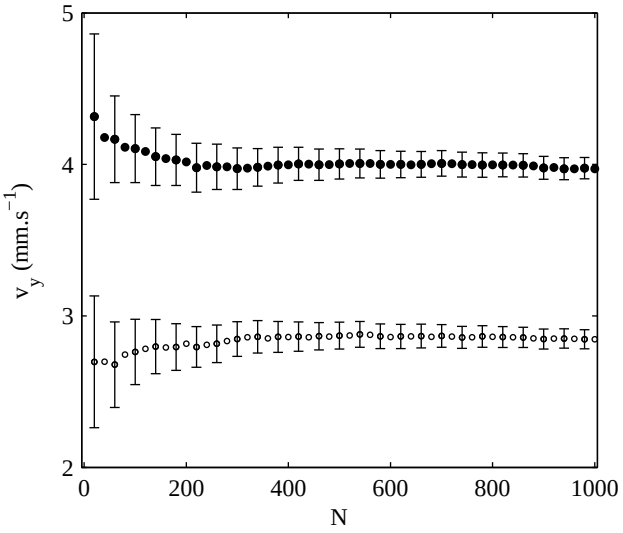

FIG. 13: Convergence of the velocity estimates as a function of the total number of pulses N taken into account in the analysis. v_y is measured at $y = 0.6$ (○) and 0.8 mm (●) for $v_0 = 23.5$ mm.s^{-1}.

VI. APPLICATION TO A COMPLEX FLUID

A. The lyotropic lamellar phase under study

Let us now turn to an application of high-frequency USV to a complex fluid. We chose to test USV in a lyotropic lamellar phase composed of SDS (6.5 % wt.), octanol (7.8 % wt.) and brine (20 g.L^{-1} NaCl). This surfactant mixture is known to display a series of structural shear-induced transitions [50, 51, 52]. At equilibrium, the system is composed of surfactant bilayers stacked with a smectic distance of about 15 nm. Under shear flow, this lamellar phase was shown to form a closely packed assembly of multilamellar vesicles [51]. The diameter of these vesicles, commonly called "onions," is typically a few microns.

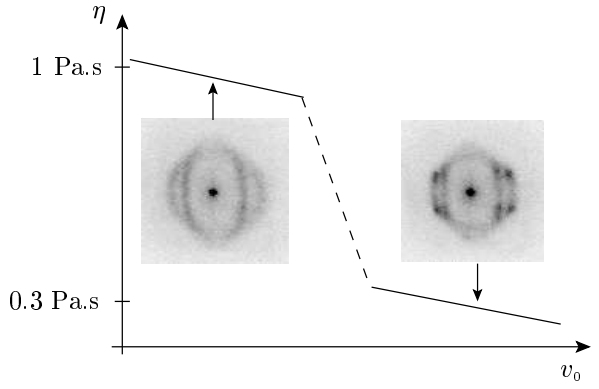

FIG. 14: Typical evolution of the viscosity η with the rotor velocity v_0 for the SDS/octanol/brine system. A shear-thinning transition occurs as v_0 is increased (dashed line). The pictures show diffraction patterns observed in the low shear regime (left) and on the high shear branch (right): a laser beam crosses the cell along the r direction and a CCD camera collects scattered light in the plane (θ, z) [51].

At low shear velocities, the diffraction pattern observed with light scattering is an isotropic ring indicating the absence of any positional order. However, when the velocity v_0 is increased, Bragg peaks appear in the diffraction pattern showing the apparition of long-range order in the vesicle positions. As sketched in Fig. 14, this disorder-to-order transition corresponds to a sharp drop in the sample viscosity by a factor of about 3 [51]. Such a shear-thinning transition is also observed in colloidal suspensions and is called a "layering" transition [53]. As explained in Sec. II B, inhomogeneous velocity profiles are expected in the vicinity of this shear-induced transition where the two states (ordered and disordered states) may coexist in the gap of a Couette cell.

As for its ultrasonic behavior, the "onion" assembly does not scatter 36 MHz pulses. Thus, the lamellar phase was seeded with the polystyrene spheres used in Sec. V in order to get some speckle signal from the fluid. We checked that the "layering" transition is not significantly modified by the addition of such contrast agents. Figure 15 presents two pictures of the seeded lamellar phase as seen under crossed polarizers and after shearing: the granular texture characteristic of disordered multilamellar vesicles does not seem perturbed by the addition of polystyrene spheres at 1 % wt.

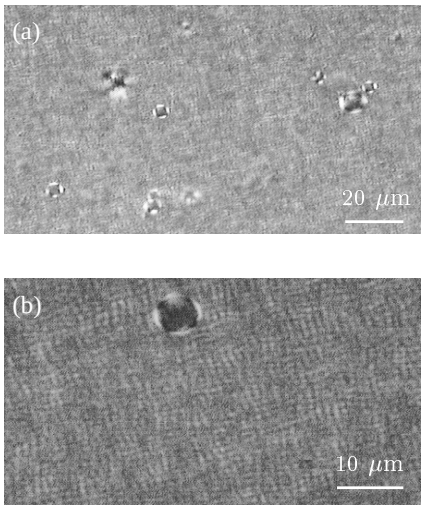

FIG. 15: Sheared lamellar phase seeded with polystyrene spheres of diameter 3–10 μm and observed under crossed polarizers at two different magnifications: (a) ×20 and (b) ×50.

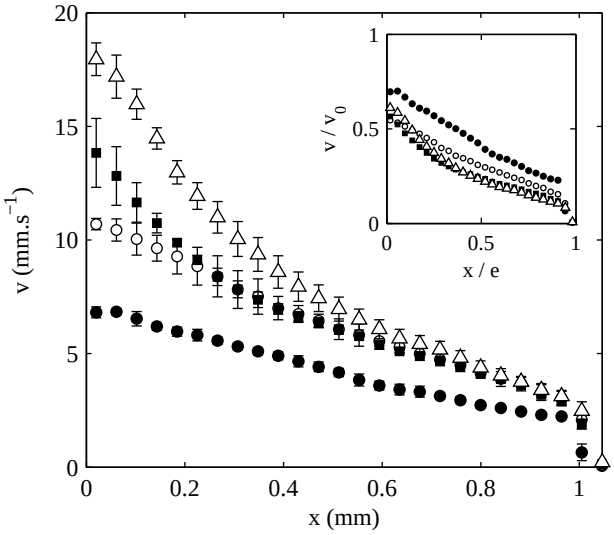

FIG. 16: Velocity profiles $v(x)$ measured in the lamellar phase for rotor velocities v_0 = 9.8 (•), 19.6 (○), 24.5 (■), and 29.4 mm.s^{-1} (△). The data were time averaged over several profiles (3 to 7 depending on v_0) obtained from series of 1000 pulses recorded in about 2 s. Error bars correspond to the standard deviation of these profiles and account mainly for temporal fluctuations of the flow. The inset shows the dimensionless data v/v_0 vs. x/e.

B. Evidence for inhomogeneous flows

As shown on Fig. 9, the sound speed of the seeded lamellar phase was measured to be $c_0 = 1495 \pm 10$ m.s^{-1}. Since the experiments and the calibration are performed at the same temperature and since the sound speeds of both fluids are the same (within less than 1 %), we used $c_0 = 1500$ m.s^{-1}, $t_s = 13.54$ μs and $\theta = 13.5°$ to obtain the velocity profiles shown in Figs. 16 and 17.

The two main features of the velocity profiles are as follows:

a. Wall slip. As clearly shown by the insets of Figs. 16 and 17, the velocity close to the walls is never equal to that of the walls. On the contrary, $v(x = 0)$ may differ from v_0 by more than 30 %. One can also notice that slip velocities are comparable at the rotor and at the stator for the smallest rotor velocity but become highly dissymmetric when $v_0 \gtrsim 20$ mm.s^{-1}. A detailed study of wall slip in this system is left for future work.

b. Shear banding. Figure 16 also unveils the presence of shear bands when $v_0 \gtrsim 20$ mm.s^{-1}. A highly sheared band nucleates close to the rotor and progressively fills the gap as v_0 is increased (see Fig. 17 for the highest velocities). The shear rate in the high shear band is about three times larger than that in the low shear band. This ratio remains roughly constant as long as two bands coexist. For $v_0 \simeq 70$ mm.s^{-1}, the highly sheared region has invaded the whole gap. When $v_0 \gtrsim 70$ mm.s^{-1}, the flow is laminar again and looks similar to that observed before the "layering" transition at $v_0 \lesssim 20$ mm.s^{-1}.

Simultaneously to the present ultrasonic measurements, DLS data obtained in our group have confirmed the existence of shear-banded flows and strong wall slip effects in the same lamellar phase without seeding polystyrene particles [54]. This last observation shows *a posteriori* that our "contrast agents" do not perturb the flow and can be treated as simple Lagrangian tracers. Both USV and DLS data are in good qualitative agreement with classical theoretical pictures of shear-banded flows [14, 55]. Our purpose here is only to show the relevance of high-frequency USV in the field of sheared complex fluids and a more quantitative analysis of shear banding in light of DLS results can be found in Ref. [54].

C. Dynamical measurements during a transient

Finally let us show how USV may be used to follow the dynamics of a complex fluid under shear. Until now, we have considered time-averaged velocity profiles. However, during the "layering" transition, noticeable fluctuations of the flow field occur and result in large error bars for $v_0 = 24.5$ or 29.4 mm.s^{-1} for instance. Actually, some very rich dynamics were reported in this sheared lamellar phase when the *torque* applied on the rotor is imposed instead of the *velocity* v_0 [19]. In that case, the viscosity $\eta(t)$ displays large, complex fluctuations on long time scales of the order of 100 s. Similar (although faster) temporal behaviors were also observed in other surfactant systems [17, 18].

The origin of these fluctuations and their precise statistical properties remain unclear. One possibility is that the flow presents shear bands that may couple to each

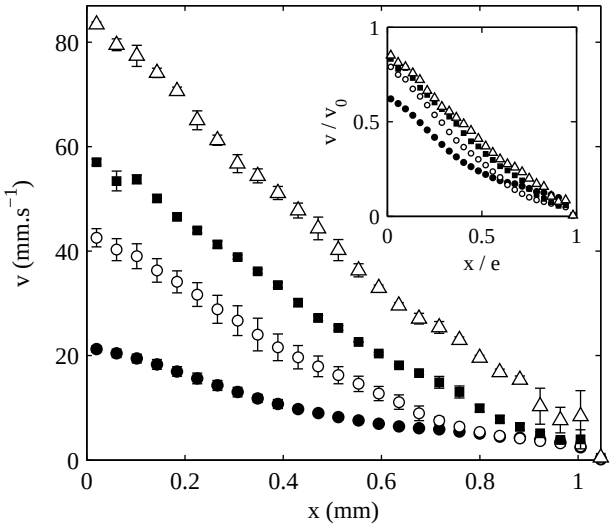

FIG. 17: Same as Fig.16 but with $v_0 = 34.3$ (•), 53.8 (○), 68.5 (■), and 97.9 mm.s^{-1} (△).

other and lead to the observed behavior of the viscosity. Thus the dynamics could be not only temporal as observed on $\eta(t)$ but also spatial as suggested in Ref. [20].

Figure 18 shows a transient regime recorded after the torque applied to the rotor was suddenly increased from 83 to 87 mN at time $t = 0$. The response of the rotor velocity $v_0(t)$ is shown in Fig. 18(a) [56]. A maximum of about 38 mm.s^{-1} is reached at $t \simeq 300$ s before $v_0(t)$ slowly relaxes with small fluctuations. Velocity profiles recorded during that transient show that: (i) during the initial increase of $v_0(t)$, a shear-banded flow is generated with *three* bands: two highly sheared bands at both the rotor and the stator and a low shear region in between (see Fig. 18(b)–(d)); (ii) the band located at the stator disappears when $v_0(t)$ decreases, leaving only *two* bands similar to Figs. 16 and 17 (see Fig. 18(e)–(f)); (iii) states where the highly sheared band almost disappears can be observed (see Fig. 18(g)) even though the rotor velocity $v_0 \gtrsim 28$ mm.s^{-1} indicates that a band should extend over almost half the gap if the average picture at imposed v_0 remained valid when the torque is imposed (see the △ symbols corresponding to $v_0 = 29.4$ mm.s^{-1} in Fig. 16).

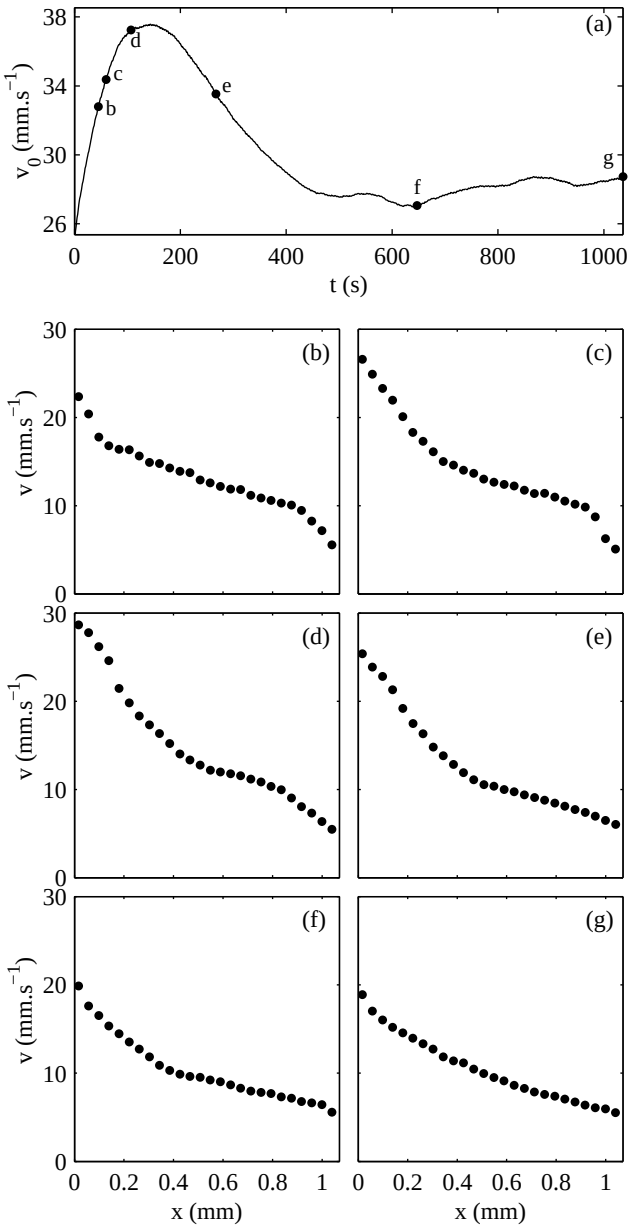

FIG. 18: Transient regime observed when the torque is increased from 83 to 87 mN at $t = 0$. (a) Velocity v_0 of the rotor as a function of time t. Bullets (•) correspond to the points where the velocity profiles shown in (b)–(g) were measured: (b) $t = 45$ s, (c) $t = 60$ s, (d) $t = 107$ s, (e) $t = 267$ s, (f) $t = 647$ s, and (g) $t = 1036$ s. The velocity profiles were obtained from series of 800 pulses recorded in 1.6 s.

VII. DISCUSSION AND CONCLUSIONS

A. Summary

The above results show that high-frequency USV is a powerful tool for measuring velocity profiles in sheared complex fluids. We have successfully tested the technique on a lyotropic lamellar phase that undergoes a shear-induced "layering" transition.

When the rotor velocity, *i.e.* the global shear rate, is imposed, shear banding is observed: time-averaged velocity profiles display a highly sheared region that nucleates from the rotor and progressively invades the gap as v_0 is increased. Wall slip can also be very large especially during the transition, which makes global measurements such as the sample viscosity tricky to analyze.

Moreover, USV allowed us to record velocity profiles in 1 s typically. This acquisition time is short enough

(compared to the intrinsic time scales of our complex fluid) to follow the velocity profiles in time. We showed the existence of more complex, three-band flows during a transient at imposed torque *i.e.* imposed shear stress. This raises the question of the structure of the flow during the spontaneous oscillations of the viscosity observed in the same lamellar phase [19, 20]. USV may thus provide a "time-resolved" tool for investigating spatially the dynamical behaviors of $\eta(t)$.

B. Comparison with other local techniques

In this paper, we have shown that we were able to measure velocity profiles with a spatial resolution of about 40 μm and every 0.02–2 s. High-frequency USV compares very well with other local techniques for measuring flow fields.

LDV, or equivalently DLS, provides in principle a slightly better spatial resolution of 10–50 μm but only yields a pointlike measurement. In order to obtain a full velocity profile with LDV or DLS, one has to mechanically scan the whole gap of the cell [27]. This usually takes about 1 min and may raise major interpretation problems when the flow evolves on time scales shorter than 1 min.

NMR appears as a very promising technique for complex fluids [6, 25, 26] since no seeding is required and two-dimensional images of the flow are obtained. However, acquisition times are rather long too (from about 20 s to more than an hour depending on the number of points in the image), making it rather difficult to access dynamical local information.

The main drawback of USV is that it needs a good control of the scattering properties of the fluid and that it may require that the flow be seeded with contrast agents. Unless their mechanical properties is strictly controlled, most concentrated suspensions or emulsions will lead to multiple scattering of high-frequency pulses. Thus, further application of USV to other complex fluids will involve a careful study of their acoustic properties. However, we believe that USV is likely to extend the range of complex fluids in which local measurements may be performed, in particular to optically opaque fluids.

C. Perspectives

The biggest advantage of USV lies undoubtedly in its ability to perform nonintrusive velocity measurements fast enough to follow the dynamics of complex fluids under low shear. In principle, in an ideal scattering environment, the temporal resolution of USV could even get as short as 1 ms per measurement.

Future research directions on USV are as follows: (i) more measurements on seeded lamellar phases will be performed and compared to DLS data; more precisely, we will focus on the spatio-temporal flow dynamics in regimes where sustained oscillations of the viscosity are observed; (ii) we will investigate shear flows of other fluids such as emulsions, gels, or granular pastes; (iii) we also intend to apply high-frequency USV to the case of very small deformations in order to perform some "local linear rheology" and understand how a complex fluid starts to flow in the transition from linear to nonlinear rheology.

Acknowledgments

The authors wish to thank the "Cellule Instrumentation" at CRPP for designing and building the mechanical parts of the experimental setup. We are very grateful to D. Roux, J.-B. Salmon, and R. Wunenburger for fruitful discussions.

[1] R. G. Larson. *The Structure and Rheology of Complex Fluids*. Oxford University Press, 1999.

[2] M. E. Cates and M. R. Evans, editors. *Soft and Fragile Matter: Non Equilibrium Dynamics Metastability and Flow*. Institute of Physics Publishing (Bristol), 2000.

[3] H. Z. Cummins and E. R. Pike, editors. *Photon Correlation Spectroscopy and Velocimetry*. Plenum Press, 1977.

[4] B. J. Berne and R. Pecora. *Dynamic light scattering*. Wiley, New York, 1995.

[5] P. T. Callaghan. *Principles of Nuclear Magnetic Resonance Microscopy*. Oxford University Press, 1991.

[6] A. D. Hanlon, S. J. Gibbs, L. D. Hall, D. E. Haycock, W. J. Frith, and S. Ablett. Rapid mri and velocimetry of cylindrical couette flow. *Magn. Reson. Imaging*, 16:953–961, 1998.

[7] I. A. Hein and W. D. O'Brien. Current time-domain methods for assessing tissue motion by analysis from reflected ultrasound echoes — a review. *IEEE Trans. Ultrason. Ferroelec. Freq. Contr.*, 40:84–102, 1993.

[8] J. A. Jensen. *Estimation of Blood Velocities Using Ultrasound*. Cambridge University Press, 1996.

[9] D. J. Tritton. *Physical Fluid Dynamics*. Oxford Science Publications, 1988.

[10] H. A. Barnes. A review of the slip (wall depletion) of polymer solutions, emulsions and particle suspensions in viscometers: Its cause, character, and cure. *J. Non-Newtonian Fluid Mech.*, 56:221–251, 1995.

[11] R. G. Larson, E. S. G. Shaqfeh, and S. J. Muller. A purely elastic transition in taylor-couette flow. *J. Fluid Mech.*, 218:573–600, 1990.

[12] A. Groisman and V. Steinberg. Mechanism of elastic instability in couette flow of polymer solutions: Experiment. *Phys. Fluids*, 10:2451–2463, 1998.

[13] J. D. Goddard. Material instability in complex fluids. *Annu. Rev. Fluid Mech.*, 35:113–133, 2003.

[14] A. Spenley, M. E. Cates, and T. C. B. McLeish. Nonlinear

rheology of wormlike micelles. *Phys. Rev. Lett.*, 71:939–942, 1993.

[15] A. Spenley, X. F. Yuan, and M. E. Cates. Nonmonotonic constitutive laws and the formation of shear-banded flows. *J. Phys. II France*, 6:551–571, 1996.

[16] G. Porte, J.-F. Berret, and J. L. Harden. Inhomogeneous flows of complex fluids: mechanical instability versus non-equilibrium phase transition. *J. Phys. II France*, 7:459–472, 1997.

[17] E. K. Wheeler, P. Fischer, and G. G. Fuller. Time-periodic flow induced structures and instabilities in a viscoelastic surfactant solution. *J. Non-Newtonian Fluid Mech.*, 75:193–208, 1998.

[18] R. Bandyopadhyay and A. K. Sood. Chaotic dynamics in shear-thickening surfactant solutions. *Europhys. Lett.*, 56:447–453, 2001.

[19] A.-S. Wunenburger, A. Colin, J. Leng, A. Arnéodo, and D. Roux. Oscillating viscosity in a lyotropic lamellar phase under shear flow. *Phys. Rev. Lett.*, 86:1374–1377, 2001.

[20] J.-B. Salmon, A. Colin, and D. Roux. Dynamical behavior of a complex fluid near an out-of-equilibrium transition: Approaching simple rheological chaos. *Phys. Rev. E*, 66:031505, 2002.

[21] V. Schmitt, F. Lequeux, A. Pousse, and D. Roux. Flow behaviour and shear-induced transition near an isotropic–nematic transition in equilibrium polymers. *Langmuir*, 10:955–961, 1994.

[22] E. Cappelaere, J.-F Berret, J.-P. Decruppe, R. Cressely, and P. Lindner. Rheology, birefringence, and small-angle neutron scattering in a charged micellar system: Evidence of a shear-induced phase transition. *Phys. Rev. E*, 56:1869–1878, 1997.

[23] E. Eiser, F. Molino, and G. Porte. Non homogeneous textures and banded flows in a soft cubic phase under shear. *Phys. Rev. E*, 61:6759–6764, 2000.

[24] D. M. Mueth, G. F. Debrégeas, G. S. Karczmar, P. J. Eng, S. R. Nagel, and H. M. Jaeger. Signatures of granular microstructure in dense shear flows. *Nature*, 406:385–389, 2000.

[25] R. W. Mair and P. T. Callaghan. Observation of shear banding in wormlike micelles by nmr velocity imaging. *Europhys. Lett.*, 36:719–724, 1996.

[26] M. M. Britton and P. T. Callaghan. Shear banding instability in wormlike micellar solutions. *Eur. Phys. J. B*, 7:237–249, 1999.

[27] J.-B. Salmon, S. Manneville, A. Colin, and B. Pouligny. An optical fiber based interferometer to measure velocity profiles in sheared complex fluids. *Eur. Phys. J. AP*, 22:143–154, 2003.

[28] J.-B. Salmon, A. Colin, S. Manneville, and F. Molino. Velocity profiles in shear-banding wormlike micelles. *Phys. Rev. Lett.*, 90:228303, 2003.

[29] A. D. Pierce. *Acoustics. An Introduction to Its Physical Principles and Applications*. American Institute of Physics, 1994.

[30] N. Mordant, O. Michel, and J.-F. Pinton. Continuous tracking of an ultrasonic doppler shift: signal processing technique and experimental applications. *J. Acoust. Soc. Am.*, 112:108–119, 2002.

[31] Y. Takeda. Velocity profile measurement by ultrasonic doppler method. *Exp. Therm. Fluid Sci.*, 10:444–453, 1995.

[32] Y. Takeda. Quasi-periodic state and transition to turbulence in a rotating couette system. *J. Fluid Mech.*, 389:81–99, 1999.

[33] I. Peschard, P. Le Gal, and Y. Takeda. On the spatio-temporal structure of cylinder wakes. *Exp. Fluids*, 26:188–196, 1999.

[34] D. Brito, H.-C. Nataf, P. Cardin, J. Aubert, and J.-P. Masson. Ultrasonic doppler velocimetry in liquid gallium. *Exp. Fluids*, 31:653–663, 2001.

[35] B. Ouriev and E. J. Windhab. Rheological study of concentrated suspensions in pressure-driven shear flow using a novel in-line ultrasound doppler method. *Exp. Fluids*, 32:204–211, 2002.

[36] O. Bonnefous and P. Pesqué. Time domain formulation of pulse-doppler ultrasound and blood velocity estimation by cross-correlation. *Ultrason. Imaging*, 8:73–85, 1986.

[37] S. G. Foster, P. M. Embree, and W. D. O'Brien. Flow velocity profile via time-domain correlation: error analysis and computer simulation. *IEEE Trans. Ultrason. Ferroelec. Freq. Contr.*, 37:164–175, 1990.

[38] K. W. Ferrara and V. R. Algazi. A theoretical and experimental analysis of the received signal from disturbed blood flow. *IEEE Trans. Ultrason. Ferroelec. Freq. Contr.*, 41:172–1184, 1994.

[39] S. Kaisar Alam and K. J. Parker. The butterfly search technique for estimation of blood velocity. *Ultrasound Med. Biol.*, 21:657–670, 1995.

[40] L. N. Bohs, B. H. Friemel, and G. E. Trahey. Experimental velocity profiles and volumetric flow via two-dimensional speckle tracking. *Ultrasound Med. Biol.*, 21:885–898, 1995.

[41] Y. Ozaki, T. Kawaguchi, Y. Takeda, K. Hishida, and M. Maeda. High time resolution ultrasonic velocity profiler. *Exp. Therm. Fluid Sci.*, 26:253–258, 2002.

[42] L. Sandrin, S. Manneville, and M. Fink. Ultrafast two-dimensional ultrasonic speckle velocimetry: A tool in flow imaging. *Appl. Phys. Lett.*, 78:1155–1157, 2001.

[43] S. Manneville, L. Sandrin, and M. Fink. Investigating a stretched vortex with ultrafast two-dimensional ultrasonic speckle velocimetry. *Phys. Fluids*, 13:1683–1690, 2001.

[44] D. H. Turnbull, B. G. Starkoski, K. A. Harasiewicz, J. L. Semple, L. From, A. K. Gupta, D. N. Sauder, and F. S. Foster. A 40–100 mhz b-scan ultrasound backscatter microscope for skin imaging. *Ultrasound Med. Biol.*, 21:79–88, 1995.

[45] M. Berson, J.-M. Grégoire, F. Gens, J. Rateau, F. Jamet, L. Vaillant, F. Tranquart, and L. Pourcelot. High frequency (20 mhz) ultrasonic devices: advantages and applications. *Eur. J. Ultrasound*, 10:53–63, 1999.

[46] K. W. Ferrara, B. G. Zagar, J. B. Sokil-Melgar, R. H. Silverman, and I. M. Aslanidis. Estimation of blood velocity with high frequency ultrasound. *IEEE Trans. Ultrason. Ferroelec. Freq. Contr.*, 43:149–157, 1996.

[47] D. A. Christopher, P. N. Burns, B. G. Starkoski, and F. S. Foster. A high-frequency pulsed-wave doppler ultrasound system for the detection and imaging of blood flow in the microcirculation. *Ultrasound Med. Biol.*, 23:997–1015, 1997.

[48] A. Echevarría, J. R. Leiza, J. C. de la Cal, and J. M. Asua. Molecular-weight distribution control in emulsion polymerization. *AIChE J.*, 44:1667–1679, 1998.

[49] S. Sugiura, M. Nakajima, and M. Seki. Preparation of monodispersed polymeric microspheres over 50 microns employing microchannel emulsification. *Ind. Eng. Chem.*

Res., 41:4043–4047, 2002.

[50] D. Roux, F. Nallet, and O. Diat. Rheology of lyotropic lamellar phases. *Europhys. Lett.*, 24:53–58, 1993.

[51] O. Diat, D. Roux, and F. Nallet. Layering effect in a sheared lyotropic lamellar phase. *Phys. Rev. E*, 51:3296–3299, 1995.

[52] P. Sierro and D. Roux. Structure of a lyotropic lamellar phase under shear. *Phys. Rev. Lett.*, 78:1496–1499, 1997.

[53] B. J. Ackerson and P. N. Pusey. Shear-induced order in suspensions of hard spheres. *Phys. Rev. Lett.*, 61:1033–1036, 1988.

[54] J.-B. Salmon, S. Manneville, and A. Colin. Shear banding in a lyotropic lamellar phase. part 1: Time-averaged velocity profiles. *Phys. Rev. E*, 2003. in press, E-print cond-mat/0307608.

[55] P. D. Olmsted and C.-Y. D. Lu. Coexistence and phase separation in sheared complex fluids. *Phys. Rev. E*, 56:R55–R58, 1997.

[56] Animations of the velocity profiles are available at: `http://www.crpp-bordeaux.cnrs.fr/~sebm/usv`.